

Invasion of homogeneous and polyploid populations in nutrient-limiting environments

Gregory J. Kimmel¹, Mark Dane², Laura Heiser^{2,1}, Philipp M. Altrock¹ and Noemi Andor¹

¹Department of Integrated Mathematical Oncology, Moffitt Cancer Center, Tampa, FL, USA ²Department of Biomedical Engineering, OHSU Center for Spatial Systems Biomedicine, Knight Cancer Institute, Oregon Health & Sciences University, Portland, OR, USA

Abstract

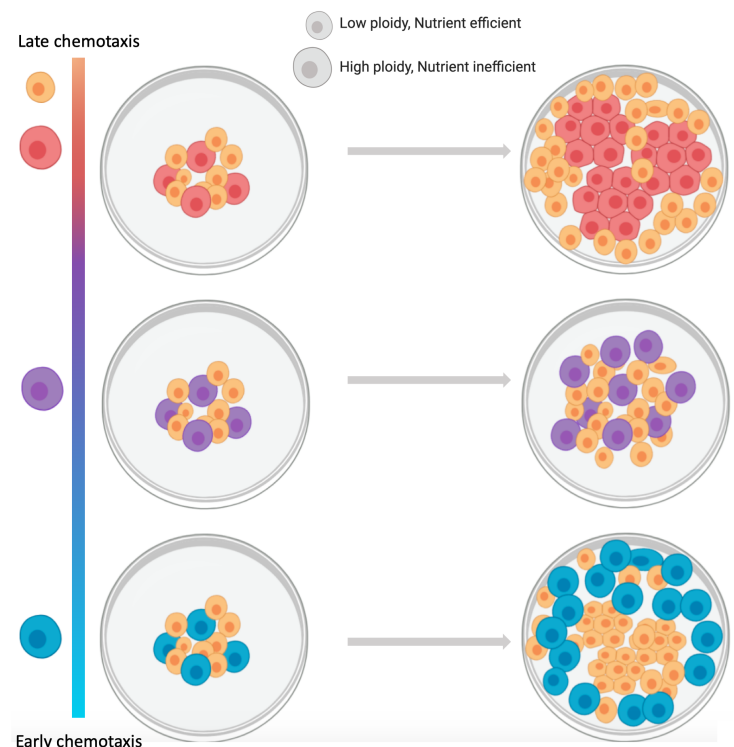
Breast cancer progresses in a multistep process from primary tumor growth and stroma invasion to metastasis. Progression is accompanied by a switch to an invasive cell phenotype. Nutrient-limiting environments exhibit chemotaxis with aggressive morphologies characteristic of invasion. The mTOR pathway senses essential nutrients, informing the cell to respond with either increased chemotaxis and nutrient uptake or cell cycle progression. Randomized clinical trials have shown that mTOR inhibitors (mTOR-I) improve the outcome of metastatic breast cancer patients. However, there are considerable differences between and within tumors that impact the effectiveness of mTOR-I, including differences in access to nutrients. It is unknown how co-existing cells differ in their response to nutrient limitations and how this impacts invasion of the metapopulation as a whole. We integrate modeling with microenvironmental perturbations data to investigate invasion in nutrient-limiting environments inhabited by one or two cancer cell subpopulations. Hereby subpopulations are defined by their energy efficiency and chemotactic ability. We calculate the invasion-distance traveled by a homogeneous population. For heterogeneous populations, our results suggest that an imbalance between nutrient efficacy and chemotactic superiority accelerates invasion. Such imbalance will segregate the two populations spatially and only one type will dominate at the invasion front. Only if these two phenotypes are balanced do the two populations compete for the same space, which decelerates invasion. We investigate ploidy as a candidate biomarker of this phenotypic heterogeneity to discern circumstances when inhibiting chemotaxis amplifies internal competition and decelerates tumor progression, from circumstances that render clinical consequences of chemotactic inhibition unfavorable.

Significance: A better understanding of the nature of the double-edged sword of high ploidy is a prerequisite to personalize combination-therapies with cytotoxic drugs and inhibitors of signal transduction pathways such as MTOR-Is.

Introduction

Invasion and infiltration are hallmarks of advanced cancers, including breast cancer, and accumulating evidence suggests that invasive subclones arise early during tumor evolution [1]. MTOR inhibitors (mTOR-I) significantly decrease migration of breast cancer cells in a dose-dependent manner [2]. A meta-analysis of four randomized clinical trials concluded that adjuvant therapy with mTOR-Is, such as rapamycin, benefits metastatic luminal breast cancer patients [3]. Rapamycin inhibits cell motility by a mechanism similar to that by which it inhibits cell proliferation [4], suggesting that the mTOR pathway lies at the intersection of a cell's decision between proliferation and migration.

The extracellular matrix (ECM) provides structural support for cells and plays an important role in tumor cell migration. Some ECM proteins, such as fibronectin and vitronectin [5], bind soluble growth factors and regulate their distribution to the cells [6]. Importantly, binding to the ECM can cause soluble factors to act and signal as solid-phase ligands. Proteolytic degradation of these ECMs creates chemotactic and haptotactic gradients causing cells to invade in a directed fashion along the ECM [7], with minimal interference from chemokinetic (i.e. random) movement [8]. Several of these matrix proteins stimulate cell-motility through integrin receptors [9, 10]. The microenvironment microarray (MEMA) plat-



Kimmel *et al.*

form allows for combinations of ECMs and ligands to be evaluated for their impact on cellular phenotypes [11, 12]. Hereby, insoluble ECM proteins are printed on a solid substrate to form spots upon which cells are grown. Soluble factors are added to the culture medium within each well of a multi-well plate. These factors include hepatocyte growth factor (HGF), a soluble ligand involved in the regulation of breast cancer cell proliferation and invasion [5, 13].

Infiltrating and invasive phenotypes are often observed among high-ploidy cells. Converging evidence from different cancer types, including colorectal-, breast-, lung- and brain cancers, suggests a strong enrichment of high ploidy cells among metastatic lesions as compared to the primary tumor [14, 15]. Even in normal development: trophoblast giant cells - the first cell type to terminally differentiate during embryogenesis - are responsible for invading the placenta and these cells often have hundreds of copies of the genome [16]. Coexistence of cancer cells at opposite extremes of the ploidy spectrum occurs frequently in cancer and is often caused by whole genome doubling (WGD). Similar to infiltration, the timing of WGD is early in tumor progression across several cancer types [17, 18], including breast cancer. Tetraploid cells resulting from WGD often lose regions of the genome, giving rise to poly-aneuploid cancer cells (PACCs). Multiple studies have described a minority population of PACCs with an unusual resilience to stress [19–21]. A very recent investigation of evolutionary selection pressures for WGD suggests that it mitigates the accumulation of deleterious somatic alterations [22]. However, it is not clear what costs cells with a duplicated genome pay for this robustness.

To address this question, we developed a mathematical model of co-evolving tetraploid and diploid clones under various energetic contingencies. We calibrate the model to recapitulate doubling times and spatial growth patterns measured for the HCC1954 ductal breast carcinoma cell line via MEMA profiling. This includes exposure of HCC1954 cells to HGF in combination with 48 ECMs, followed by multi-color imaging [11]. Our results show that long-term coexistence of diploid and tetraploid clones occurs when sensitivity of the latter to energy scarcity is well-correlated to their chemotactic ability to populate new terrain. Higher energy uniformity throughout population expansion steers selection in favor of the diploid clone, by minimizing the fitness gain the tetraploid clone gets from its chemotactic superiority. Better understanding of how these two phenotypes co-evolve is necessary to develop therapeutic strategies that suppress slowly-proliferating, invasive cells before cytotoxic therapy favors them.

Materials and Methods

Overall model design

We modeled growth dynamics in polyploid populations of various subpopulation compositions. At the core of our model lies the assumption that chemotactic response to an energy gradient is a function of the cell's energetic needs. This trade-off implies that heterogeneous populations will segregate spatially, with more energy demanding cells leading the front of tumor growth and invasion.

We model competition for energy in a heterogeneous population, consisting of goer and grower subpopulations, to predict their behavior during plentiful and energy sparse conditions. Sensitivity to the available energy is modeled via a Michaelis-Menten type equation with coefficients Φ_i that determine the amount of energy population i needs for a half-maximal growth rate. We assume both goer and grower have the same random cell motility coefficient Γ , the same chemotactic coefficient χ and maximal growth rate λ . However, their chemotactic motion is asymmetrically sensitive to the amount of energy available. This is accounted for by Ξ_i . The goers (U) are more motile and require more energy compared to the growers (V). This manifests itself mathematically via the parameter relations $\Phi_U > \Phi_V$ and $\Xi_U < \Xi_V$.

Quantitative estimates of how a cell's growth rate and motility depends on energy availability have been described [23–25]. Energetic resources come in various forms, and the identities of the limiting resources that ultimately drive a cell's fate decision vary in space and time. We used MEMA profiling to investigate what likely is only a narrow range of that variability – 48 HGF-exposed ECMs. HGF stimulates both growth and migration of epithelial and endothelial cells in a dose-dependent manner, whereby maximal growth-stimulating effects have been reported at concentrations twice as high as concentrations that maximize migration [26]. In line with these reports, our model implements a shift from proliferation to migration as resources get depleted.

Mathematical models of a dichotomy between proliferation and migration are numerous [27–29], but whether the two phenotypes are indeed mutually exclusive remains controversial [30]. Our efforts to use mathematical modeling to inform what cost high-ploidy cells (goers) pay for their robustness builds upon these prior works. We extend it by accounting for differences in the rate at which cells consume energy (a) and differences between media in the rate at which energy diffuses (coefficient Γ_E). For mid-range energy diffusion coefficients our model describes directed cell motility in response to a gradient of a soluble attractant, i.e. chemotaxis. By contrast, small values of Γ_E approximate cell motility towards insoluble attractants, i.e. haptotaxis. As such, the chosen value for Γ_E sets where along the continuum between haptotaxis and chemotaxis directed cell movement resides. A special case applies when the energy diffusion coefficient is very large relative to cell movement, in which case neither chemotaxis nor haptotaxis occurs. All these energetic contingencies determine whether phenotypic differences between goers and growers manifest as such, and explain why non-proliferative arrested cells can have the same motility as cycling cells [30]. A future extension will be to integrate our model of the potential cost of high ploidy with existing Markov models of the robustness benefits it can provide against deleterious mutations [22, 31, 32]. With a better understanding of the nature of the double-edged sword of high ploidy, we aim to contribute towards personalized combination-therapies with cytotoxic drugs and inhibitors of signal transduction pathways such as MTOR-Is.

Quick guide to equations

Our model assumes that the energy diffusion coefficient Γ_E depends on the type of media or surface upon which the cells grow. We also suppose that energy is consumed in proportion to the amount of cells present. For cell motility, we assume it is driven both by random cell motion and chemotaxis. This leads to our general coupled system:

$$\frac{\partial \tilde{E}}{\partial t} = \underbrace{\Gamma_E \nabla^2 \tilde{E}}_{\text{Nutrient diffusion}} - \underbrace{\delta \tilde{E}(U + V)}_{\text{Nutrient consumption}}, \quad (1a)$$

$$\frac{\partial U}{\partial t} = \underbrace{\Gamma_U \nabla^2 U}_{\text{Random motion}} - \underbrace{\chi \nabla \cdot \frac{U \nabla \tilde{E}}{\Xi_U + \tilde{E}}}_{\text{Chemotaxis}} + \underbrace{\lambda \frac{\tilde{E}}{\Phi_U + \tilde{E}}}_{\text{Energy-dep. growth}} U \underbrace{\left(1 - \frac{U + V}{K}\right)}_{\text{Contact inhibition}}, \quad (1b)$$

$$\frac{\partial V}{\partial t} = \underbrace{\Gamma_V \nabla^2 V}_{\text{Random motion}} - \underbrace{\chi \nabla \cdot \frac{V \nabla \tilde{E}}{\Xi_V + \tilde{E}}}_{\text{Chemotaxis}} + \underbrace{\lambda \frac{\tilde{E}}{\Phi_V + \tilde{E}}}_{\text{Energy-dep. growth}} V \underbrace{\left(1 - \frac{U + V}{K}\right)}_{\text{Contact inhibition}}. \quad (1c)$$

The system (1) is defined on a dish of radius R subject to no-flux boundary conditions. We assume the cells U, V are initially concentrated at the center with radius $\rho_0 \leq R$ and initial concentrations U_0, V_0 . Further, we assume that the energy density is uniformly distributed on the plate with initial value E_0 . All parameters except otherwise stated are independent of any of the state variables (\tilde{E}, U, V). The energy is consumed at rate δ . Both cells can divide at the maximal rate λ , but are restricted by the energy density \tilde{E} . The cells can locally grow to a local maximal density given by K . This parameter is often cell line-dependent and is related to contact inhibition and a cell's ability to grow on top of each other.

We now convert our system to dimensionless form that was used for all subsequent simulations and analysis via appropriate re-scaling (Appendix),

$$\frac{\partial E}{\partial \tau} = \gamma_E \nabla^2 E - aE(u + v), \quad (2a)$$

$$\frac{\partial u}{\partial \tau} = \nabla \cdot \left(b \nabla u - u \frac{\nabla E}{\xi_U + E} \right) + \frac{E}{\phi_U + E} u(1 - u - v), \quad (2b)$$

$$\frac{\partial v}{\partial \tau} = \nabla \cdot \left(b \nabla v - v \frac{\nabla E}{\xi_V + E} \right) + \frac{E}{\phi_V + E} v(1 - u - v), \quad (2c)$$

Hereby re-scaling simplified the system from thirteen (ten parameters and three initial conditions) to nine (seven parameters and two initial conditions), with dimensionless variables $\gamma_E = \Gamma_E/\chi$, $a = \delta K/\lambda$, $b = \Gamma/\chi$, $\phi = \Phi/E_0$ and $\xi = \Xi/E_0$.

Infiltration

An important question in cancer dynamics is infiltration into and through tissue. The desire for cells to move is inherently tied to the availability of nutrients and space. To this end we define $\Psi(\tau) := [\rho(\tau) - \rho_0]/\rho_0$ where $\rho(0) = \rho_0$, the initial radius of cell seeding density. Ψ can be thought of as a non-dimensional measure of infiltration attained after time τ . This dimensionless measure has the added benefit of being scale-independent. An inherent difficulty with random cell motility and calculating infiltration is that the system always reaches the boundary of the dish in finite

time. Instead we will define the maximum degree of infiltration to be given by the time needed for the total energy to be below a threshold $\varepsilon \ll 1$. For simulations, we took the 1-norm $\|E\|_1 < \varepsilon = 1e-4$.

In general, the maximum degree of infiltration is difficult to predict analytically, so we will only consider the single subpopulation case when obtaining our analytical estimates. We will also make use of the simplification that most energy-type molecules (e.g. glucose) have a diffusion coefficient that is very large, relative to cell movement. This allows us to write a reduced model which has energy homogeneous in space (S3a)-(S3b).

Parameter	Symbol	Value (1)	Value (2)	Unit
Goer's seeding density	u_0	36.0 ^b	3.8	% confluence
Grower's seeding density	v_0	na	1.3	% confluence
Energy diffusion coefficient on ECM	Γ_E	9000 ^a	8982	$\mu\text{m}^2 \text{day}^{-1}$
Energy consumption rate	δ	31 ^a	23	$\text{cells}^{-1} \text{day}^{-1}$
Maximal growth rate	λ	0.56 ^b	0.56 ^b	day^{-1}
Energy needed for half-maximal growth	Φ_u	[0.01, 2] ^a	0.310	
	Φ_v	na	[0.05, 0.16]	
Chemotactic coefficient	χ	1050 ^a	1919 ^b	$\mu\text{m}^2 \text{day}^{-1}$
	ξ_u	[5, 150] ^a	[0.2, 8]	
Energy deficit inducing chemotaxis	ξ_v	na	140	
Simulation time	t	3 ^b	127	days
Characteristic length	L	[11, 97] ^b	58 ^b	μm
Radius of domain	\tilde{R}	1750 ^b	1750 ^b	μm
Seeding radius	ρ_0	175 ^b	175 ^b	μm
Growth beyond ρ_0		no	yes	

^aMaximum a posteriori estimate derived from calibration to MEMA measurements

^bExperimental measurement or configuration

Table 1. Measured and inferred simulation parameters. (1) One-population model; (2) Two-population model. Parentheses indicate ranges with multiple equally good fits. Corresponding non-dimensional parameters are shown in Supplementary Table 4.

No chemotaxis infiltration estimate

We can derive an estimate for infiltration in the absence of chemotaxis by appealing to (S3a)-(S3b). These logistic growth-reaction-diffusion models often exhibit complex dynamics. One such example is that of a traveling-wave solution, where one state, typically the stable state, travels (infiltrates) through the domain. The canonical example of this phenomenon is the Fisher-KPP. In contrast to the Fisher-KPP and other biology equations subsequently studied, our model has a decaying growth rate and so the magnitude of the non-linearity that caused the traveling wave is tending to zero. Therefore, in the classic sense, our system does not admit a traveling wave. We here extend the theory by assuming a separation of time scales between consumption of energy (e.g. decay of energy-dependent growth rate) and the speed of the traveling wave.

To begin, we make the assumptions that the wave speed is a slow function of r and τ . The solution obtained will verify that these assumptions are valid for our system. Our ansatz takes the form $u(r, \tau) = U(r - \eta\tau) = U(z)$. Note that in spatial equilibrium, $u = 1$ is stable and $u = 0$ is an unstable steady state. If the unstable state is what governs the wave speed, then the wave is said to be "pulled", otherwise it is "pushed" [33, 34]. The resulting analysis yields a coupled system of ODEs that govern the speed of the front

Kimmel *et al.*

(Appendix):

$$\frac{dE}{d\tau} = -a \left(\frac{\rho}{R} \right)^2 E, \quad (3a)$$

$$\frac{d\rho}{d\tau} = 2\sqrt{\frac{bE}{\phi + E}} - \frac{b(n-1)}{\rho}. \quad (3b)$$

We see that our assumptions on the behavior of the traveling wave are verified, since ρ is assumed much larger than 0 and $0 \ll \rho \ll R$. This shows that E is a slowly varying function of time and $\eta = d\rho/d\tau$ is a slowly varying function of time and its current distance from the center. In other words, a traveling wave will only form when the initial seeding radius is relatively large ($\rho_0 \sim 1$ was sufficient in most simulations).

Estimating the degree of infiltration from equilibration

The previous section yields a system that can be integrated to track the evolution of the cell front over time. However, we may be more interested in how far it will ultimately travel before energy exhaustion and not the speed at which it gets there. An interesting alternative to tracking the wave over time is to only assume it travels as a wave, but only record the density after the system has reached uniformity. This is possible if the death rate (which has been neglected) is much smaller than the time it would take the cells to spread uniformly. If this is the case, we can bind the degree of infiltration from only knowing the uniform value \bar{u} at the end of the experiment (see Appendix for details):

$$\rho(\tau = T) = R\sqrt{\frac{2\bar{u}}{1 + \Lambda^2}}. \quad (4)$$

, where Λ is the transition width, i.e. the length scale on which cell concentration goes from $u = 1$ to $u = 0$, and \bar{u} it is the concentration at the end of the experiment (at equilibration). Solving (4) gives us the estimated infiltration as:

$$\Psi = \frac{R}{\rho_0} \sqrt{\frac{2\bar{u}}{1 + \Lambda^2}} - 1. \quad (5)$$

Since we assume that the transition width is unknown, we can bind Ψ (or $\rho(T)$) by considering the lower and upper bounds $\Lambda = 0, 1$, respectively.

Model calibration

We calibrate the model to recapitulate doubling times and spatial growth patterns measured for the HCC1954 ductal breast carcinoma cell line via MEMA profiling. The dataset includes exposure of HCC1954 cells to HGF in combination with 48 ECMs in a DMSO environment (i.e. no drug was added to the media). Between 13 and 30 replicates of each ECM are printed on a rectangular MEMA array as circular spots (Supplementary Fig. 1A), adding up to a total of 692 spots [11].

MEMA data analysis

An average of 62 cells (90% confidence interval: 50-75) were seeded on each 350 μm spot and grown for three days. Confluence

at seeding was calculated from the ratio between the cumulative area of cells and the area of the spot (see Supplementary Fig. 1).

Quantification of segmented, multi-color imaging data obtained for each spot three days post-seeding was downloaded from Synapse (synID: syn9612057; plateID: LI8C00243; barcode: B03). We binned cells detected within a given spot according to their distance to the center of the spot and calculated the confluence of each bin (Supplementary Methods). This was then compared to the confluence obtained from the simulations as described below.

Simulation environment

Simulations were ran for three days on a circular domain with radius $R = 1750 \mu\text{m}$. Cells were seeded uniformly at the center of this domain along a radius $\rho_0 = 175 \mu\text{m}$ at 36% confluence. These two initial conditions were given by the MEMA experimental design (Supplementary Fig. 1A). To recapitulate the configuration of the MEMA profiling experiment, cells leaving the ρ_0 domain can no longer adhere to the ECM and die. This was implemented by having the carrying capacity $K(x)$ rapidly approach zero when $x > \rho_0$. This setup can have energy attract cells to the periphery of a MEMA spot and beyond. We ran 10,000 simulations at variable energy consumption rates, chemotactic coefficients, energetic sensitivities, and diffusion rates of the growth-limiting resource (i.e. ECM-bound HGF; Table 1). For each simulation/ECM pair, we compared spatial distributions of in-silico to in-vitro confluence using the Wasserstein metric [35].

The model was implemented in C++ (standard C++11). The armadillo package (ARMA version: 9.860.1) [36] was used for simulation of the PDEs. Simulations were run on a Intel Core i7 MacBook Pro, 2.6 GHz, 32 GB RAM. The source code is available at the github repository for the IMO department: [GoOrGrow](#).

Ploidy as biomarker of phenotypic divergence

RNA-Seq analysis

We identified 44 breast cancer cell lines of known ploidy [37] and with available RNA-seq data in CCLE [38]. The molecular subtype classification of all these cell lines was available from prior studies [39–42]. Of these 44 cases, four were suspension cell lines and excluded from further analysis. Of the remaining 40 cell lines, 20 originated from primary breast cancer tumors and were the focus of our analysis. Gene expression data was downloaded from CCLE. We used gene set variation analysis (GSVA) to model variation in pathway activity across cell lines [43]. Pathways for which less than ten gene members were expressed in a given cell lines were not quantified. The gene membership of 1,417 pathways was downloaded from the REACTOME database [44] (v63) for this purpose. As a surrogate for the importance of a given ECM in the HCC1954 cell line, we quantified the cumulative activity of pathways which have the corresponding ECM as a member (Supplementary Table 6).

Drug sensitivity analysis

We used Growth rate inhibition (GR) metrics as proxies of differences in drug sensitivities between cell lines. Unlike traditional drug sensitivity metrics, like the IC_{50} , GR curves account for unequal division rates, arising from biological variation or variable culture conditions – a major confounding factor of drug response [45]. Previously calculated GR curves and metrics were available for 41/44 breast cancer cell lines. A total of 46 drugs had been profiled on at least 80% of these cell lines and their GR_{AOC} drug response metric [46] was downloaded from [GRbrowser](#). For each drug we calculated the z-score of GR_{AOC} across cell lines in order to compare drugs administered at different dose ranges. Of these 46 drugs, 39 could be broadly classified into two categories as either cytotoxic (25 drugs) or inhibitors of signaling pathways (14 drugs) (Supplementary Table. 3). We then evaluated a cell line's ploidy as a predictor of its GR_{AOC} value using a linear regression model. Since molecular subtype of breast cancer cell lines is known to influence drug sensitivity we performed a multivariate analysis, including the molecular subtype as well as an interaction term between ploidy and drug category into the model.

Results

High-ploidy breast cancer cell lines have increased metabolic activity and cell motility

To better understand the phenotypic profile of high-ploidy cells, we compared the ploidy of 41 breast cancer cell lines with their response to 46 drugs. As drug response metric, we used the integrated effect of the drug across a range of concentrations estimated from the 'area over the curve' (GR_{AOC}) [45, 46]. We observed that cytotoxic drugs and drugs inhibiting signal transduction pathways were at opposite ends of the spectrum (Fig. 1A). Namely, ploidy was negatively correlated with the GR_{AOC} for several cytotoxic drugs and positively correlated with the GR_{AOC} of various mTOR inhibitors, suggesting high ploidy breast cancer cell lines tend to be resistant to DNA damaging agents, while sensitive to drugs targeting nutrient sensing and motility.

We built a multivariate regression model of drug sensitivities to test the hypothesis that the relationship between ploidy and GR_{AOC} was different for cytotoxic drugs than for inhibitors of cell signaling pathways. Molecular subtype alone (Fig. 1B), could explain 0.4% of the variability in GR_{AOC} z-scores across cell lines (adjusted R-square = 0.0044; $p = 0.026$). Including ploidy into the model did not improve its predictive accuracy (adjusted R-square = 0.0037; $p = 0.058$). However, an interaction term between ploidy and drug category (cytotoxic: 27 drugs vs. signaling: 16 drugs) increased accuracy to explain 2.6% of variability in drug sensitivity across cell lines (adjusted R-square = 0.026; $p < 1e-5$; Fig. 1C). The same improvement from an interaction term between ploidy and drug category was observed in an independent dataset of maximal inhibitory concentration (IC_{50}) values of 34 cytotoxic drugs and 51 signaling inhibitors obtained from the GDSC (Genomics of Drug Sensitivity in Cancer) database [47] (Supplementary Fig. 3).

We then focused on a subset of aforementioned 41 cell lines, namely those that had been established from primary breast cancer tumors as adherent cells (20 cell lines; Fig. 1D) and we quantified their pathway activity (see Methods). A total of 27 pathways were correlated to ploidy at a significant p-value ($|\text{Pearson } r| \geq 0.44$; $p \leq 0.05$; Supplementary Table 1). The strongest correlations were observed for metabolic pathways such as hyaluronan metabolism and metabolism of vitamins (Fig. 1E-F). Hyaluronic acid is a main component of the ECM and its synthesis has been shown to associate with cell migration [48, 49].

These results support a model that connects high ploidy with both, the chemotactic ability and metabolic energy deficit of a cell.

Infiltration of homogeneous populations in the absence of chemotaxis

An important biological question is the degree of infiltration attained by cells of a given energy deficit. That is, when seeded at the center of a cell culture dish, how far through will the cells travel before the energy has been exhausted? An analytical estimate would be useful in this regard. It would point to important scaling relationships that govern how the cell front will evolve in time. To this end, we employed the simplification that diffusion of energy molecules (e.g. glucose) is very fast relative to cell movement. This along with the assumption that the cells' movement can be approximated by a traveling wave [50] leads to the system (3a)-(3b) (Fig. 2D). These assumptions were verified by comparing the front estimates with results from the full numerical model (equations (2a) - (2c); Fig. 2A,B). These analytical solutions point to scaling relationships on the speed of the moving front. For highly efficient energy-using cell lines ($\phi \ll 1$), the front will evolve at a speed nearly independent of energy for a long time. In contrast, for large $\phi \gg 1$, the speed of the front falls off as $1/\sqrt{\phi}$. These relationships and others can be investigated and verified experimentally.

An alternative to tracking the wave over time is to assume it travels as a wave, but only record the density after the system has reached uniformity. If the death rate is much smaller than the time needed for the cells to spread uniformly, we can bind the degree of infiltration that occurred from only knowing the uniform density of cells (eq. (4); Fig. 2C).

In summary, we developed two alternative analytical expressions of the evolution of the wave front over time in the presence of a decaying energy term. The first reduced model is in decent agreement with the qualitative trends that we observed in the full numerical model. However, this expression is only valid when there is strong separation of time scales between cell movement and consumption of the available energy. The second alternative analytical expression does not make this assumption. By calculating the average concentration at equalization, we reverse engineer the approximate movement traveled by the wave before energy has been exhausted.

Infiltration of homogeneous, chemotactic populations

Assumptions made in the prior section apply to standard cell cultures of adhesive cells in a typical cell culture dish, where energetic

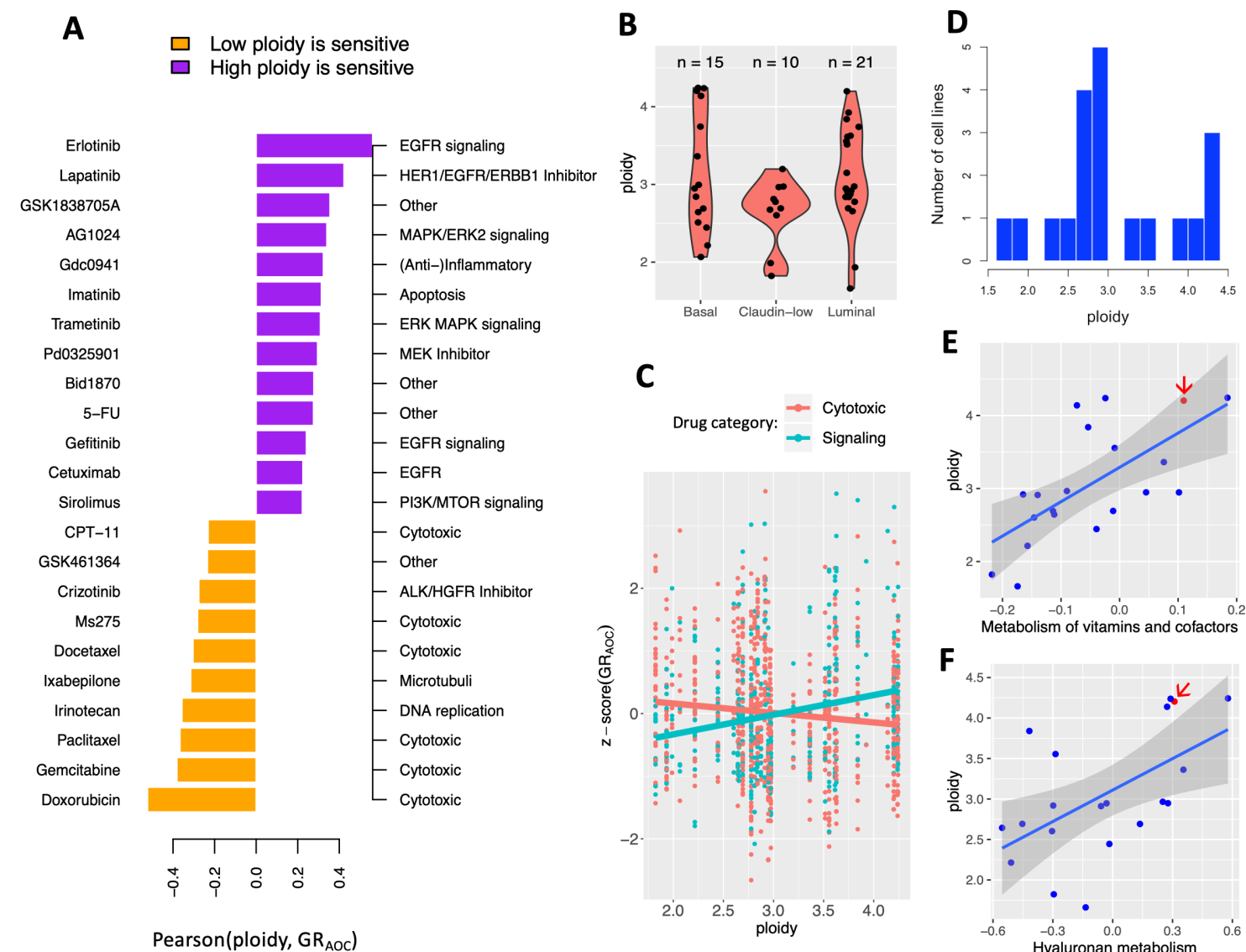


Figure 1. Ploidy, pathway activity and drug sensitivity across breast cancer cell lines from CCLE. (A) High-ploidy breast cancer cell lines are resistant to cytotoxic drugs, but tend to be more sensitive to inhibitors of mTOR, EGFR and MAPK signaling pathways. Hereby ploidy is defined as the number of chromosomes in the cell line's consensus karyotype, weighted by chromosome size. Only drugs with a Pearson correlation coefficient at or above 0.2 are shown here. (B) Distribution of ploidy within and across three molecular breast cancer subtypes. (C) Regression coefficient of ploidy as predictor of GR_{AOC} has opposite signs depending on drug category across all subtypes. (D) Distribution of ploidy across 20 primary, adherent breast cancer cell lines from CCLE. (E-F) Ploidy is correlated with the activity of pathways involved in metabolism of vitamins and cofactors (E) and Hyaluronan metabolism (F). One cell line with available MEMA profiling data – HCC1954 – is highlighted (red arrow).

resources, such as glucose, diffuse so fast that gradients cannot form. But these assumptions break down when chemotactic and haptotactic gradients cause cells to move in a directed fashion, as is the case during cellular growth on an ECM. When directed cell movement is not negligible, analytical approximations are more difficult to obtain, and numerical simulations are preferred to estimate the degree of infiltration. Fig. 1 includes HCC1954 – a near-tetraploid breast cancer cell line that has been extensively profiled, including its genome, transcriptome, methylome and drug sensitivity [37]. This list has recently been extended to include MEMA profiling [12]. We asked whether the spatial growth pattern of HCC1954 cells, as measured via MEMA profiling, can be explained by our

mathematical model.

Phenotypic profiling of HCC1954 cells in the presence of HGF was performed across multiple replicates of 48 ECMs. Cells tended to grow in a symmetric, toroidal shape (Fig. 3A), albeit considerable variability was observed across the ECMs (Fig. 3B,C). The maximum number of cells imaged at day three was 195 – close to the number of cells expected from a doubling time of approximately 43.81 hours reported for this cell line (194 cells).

Informed by this experimental setting we ran 10,000 simulations at variable energy consumption rates, chemotactic coefficients, energetic sensitivities, and diffusion rates of the growth-limiting resource (i.e. ECM-bound HGF; Table 1). For each simulation/ECM

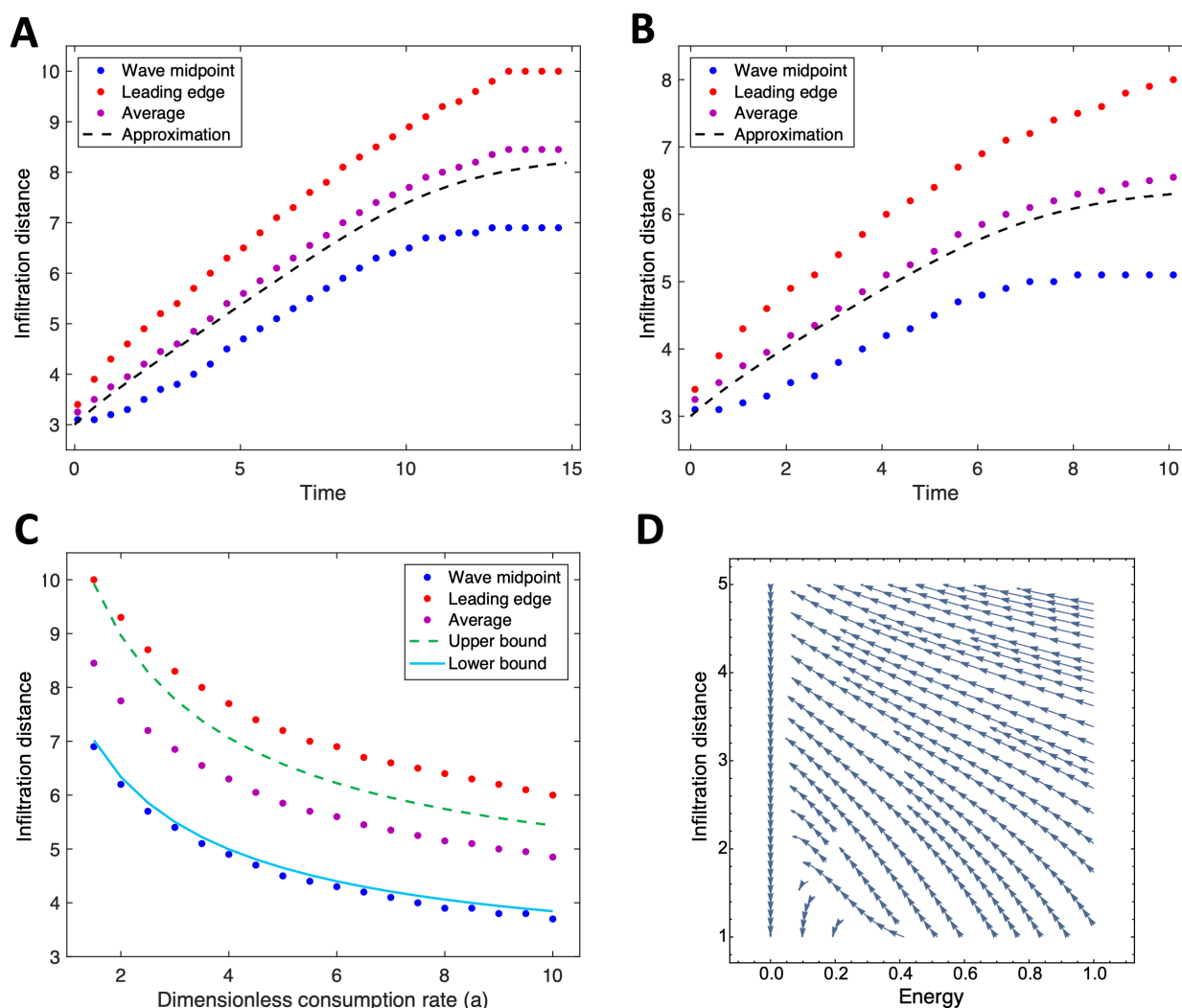


Figure 2. Comparing analytical approximations of the degree of infiltration with those obtained from simulations. (A-B) Traveling-wave solutions at energy consumption rates $a = 1.5$ (A) and $a = 3.5$ (B). (C) Upper and lower boundaries of traveling wave solutions estimated from equilibration are shown as a function of consumption rate. Approximation is found by lower and upper bound $\Lambda = 0, 1$ from equation (4). (D) Phase diagram of energy consumption and front location using the derived coupled system (3a)-(3b). (A-D) All approximations and simulations assume energy is uniformly distributed at all times, i.e. chemotaxis does not take place. Parameter values for initial seeding radius (ρ_0), dish radius (R), and sensitivity to low energy (ϕ) are set to 3, 10 and 0.05 respectively. Red = leading edge of wave (estimated by finding value of cell conc. closest to 0.01); blue = mid point of wave (estimated by finding value of cell conc. closest to 0.5); purple = average of red and blue; black lines are approximations based on analytical solutions.

pair, we compared in-silico to in-vitro growth with respect to (i) confluence (Fig. 3D) and (ii) the spatial distribution of cells using the Wasserstein metric (Fig. 3E,F).

Comparing the top 1% best fits across ECMs, we observe wide ranges of sensitivities to low energy that could explain in-vitro spatial growth patterns, while ranges of compatible energy diffusion- and chemotactic/haptotactic coefficients were more localized (Fig. 3G-I). These top fits mapped to 10 out of 48 ECMs, suggesting the chosen posterior distributions could explain a significant proportion of growth conditions on the HGF-exposed MEMA array. We observed substantial differences in chemotactic/haptotactic coefficients and energy consumption rates between ECMs (Supplementary Fig. 4). To query the biological significance of this variability we quantified the cumulative activity of pathways that use a given ECM (see Methods). We did this for each of the 10 ECMs for which

the simulations yielded a good fit. One of the five inferred model parameters – sensitivity to low energy – was correlated with RNA-seq derived pathway activity (Pearson $r = 0.724$, $p = 0.028$; Supplementary Fig. 5A). This was to a lesser extent also the case when considering each ECM alone rather than the pathways in which it is involved (Pearson $r = 0.639$; $p = 0.064$; Supplementary Fig. 5B). This result suggests that ECMs on which HCC1954 cells depend upon for growth tend to be involved in multiple active pathways in those cells.

In summary, this approach identified regions of interest in the parameter search space, allowing us to focus further simulations on biologically relevant chemotactic/haptotactic coefficients and energy diffusion rates.

Kimmel *et al.*

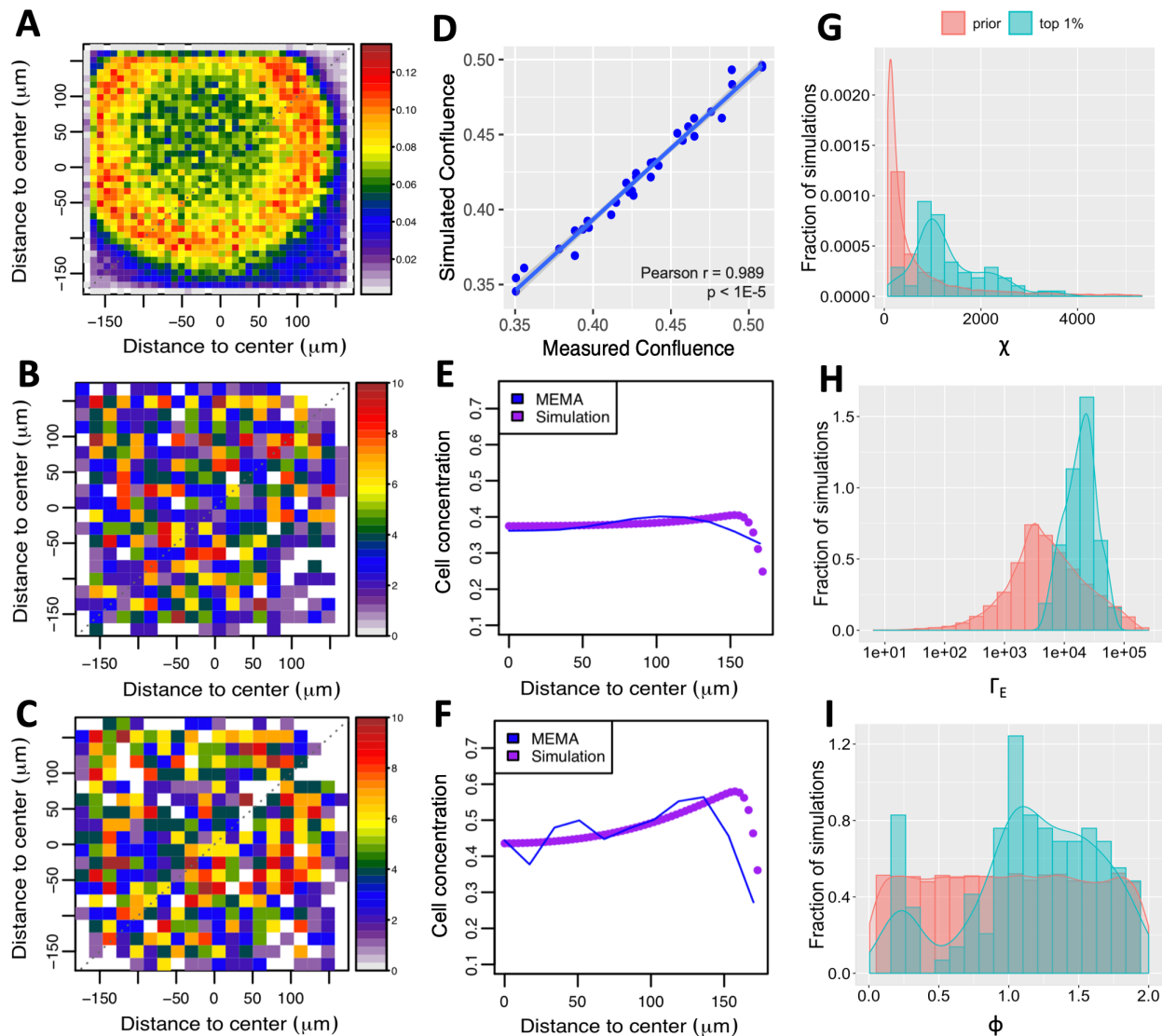


Figure 3. Model calibration using MEMA profiling of HCC1954 cells. (A) Density distribution of spatial growth patterns is shown in aggregate across all 692 HGF exposed ECM proteins. (B-C) Variability in cell growth patterns across ECMs is demonstrated via two example ECMs: COL1 (B) and SPP1 (C). (D-F) Confluence (D) and cell growth patterns (E,F) resulting from our simulations are compared to those measured in-vitro with MEMA profiling. ECM-specific parameters used in these simulations are in Supplementary Table 5. (G-I) Comparing prior- and posterior parameter space for chemotactic/haptotactic coefficient (χ) (G), energy diffusion rate (Γ_E) (H) and sensitivity to low energy (ϕ) (I).

Infiltration of heterogeneous, chemotactic populations

Growth of cells in a given ECM environment was measured across 13-30 replicates on the MEMA platform. While our model – when calibrated to the corresponding ECM environment – could explain the observed growth pattern in the majority of these replicates, a substantial fraction could not be explained by fixed choices of sensitivity to low energy and directed cell motility. One possibility that may explain this is that HCC1954 is a heterogeneous cell line, with clones of variable phenotypes co-evolving. Representation of these clones among the 62 cells that were on an average sampled for each replicate may vary (Supplementary Fig. 2). This hypothesis is supported by a bimodal distribution of DNA content observed among replicating HCC1954 cells on individual ECM spots (Fig. 4A,B), and by a bimodal posterior distribution of sensitivity to low

energy inferred during model calibration (Fig. 3I), that was not a function of the ECM (Supplementary Table 2). These observations suggest that HCC1954 is likely a polyploid cell line, i.e. clones of variable ploidies co-exist in this cell line.

To better understand the growth dynamics in a polyploid population, we used the two-subpopulation version of our model, whereby variable chemotactic abilities and energetic sensitivities of goer- and grower subpopulations compete with one another (equations (2a) - (2c)). We used fixed values for energy diffusion- and consumption rates as informed by model calibration (Fig. 3B) and varied sensitivity to low energy and chemotactic ability of both goer and grower, subject to equations (2a) - (2c) (Table 1). We initially used the same spatial and temporal domains as during model calibration, but concluded that the implied duration of the experiment (3 days) was too short for dynamics between the two populations to manifest. Each

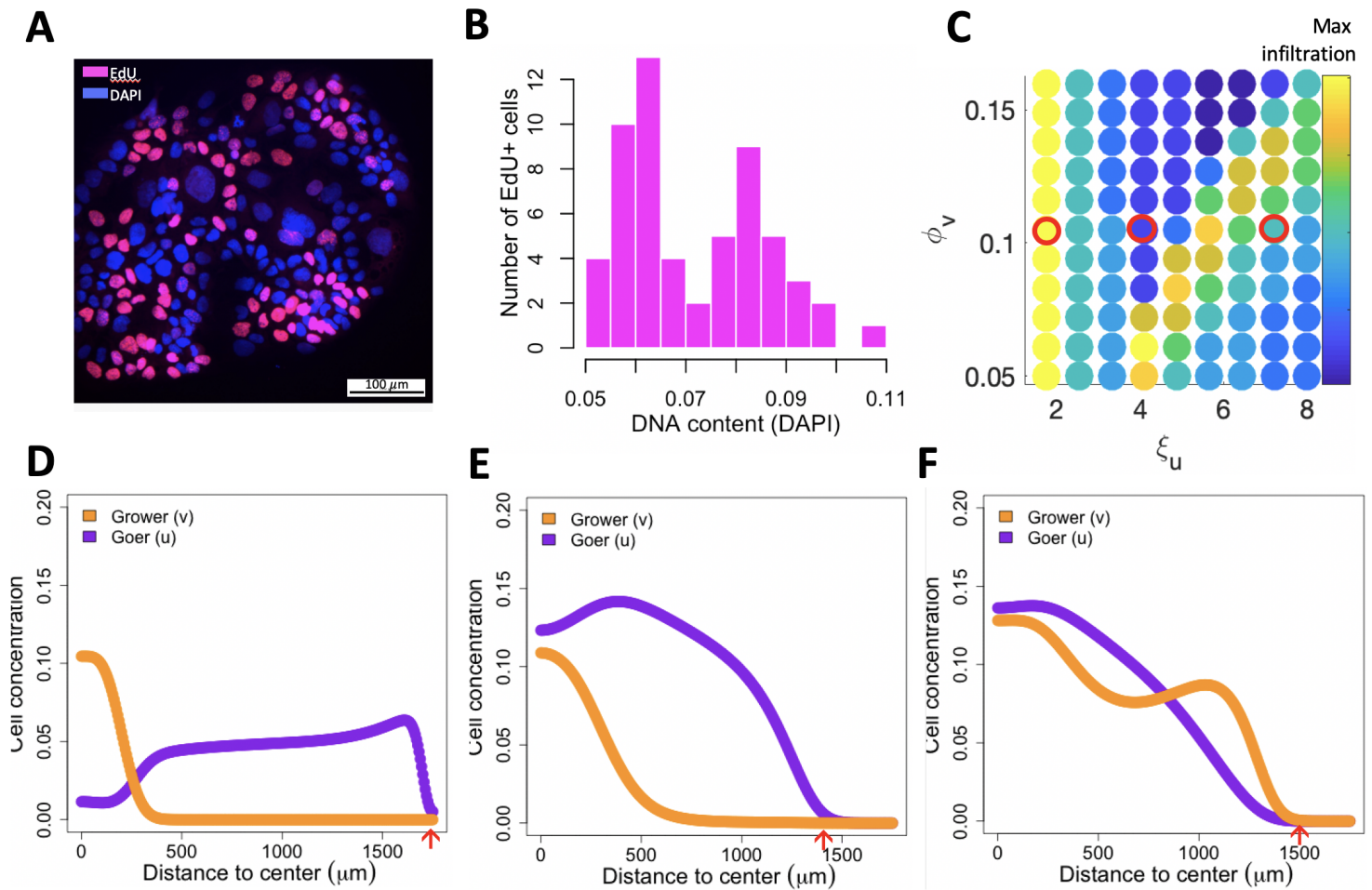


Figure 4. Internal competition of co-existing subpopulations for same space slows down invasion of the metapopulation. (A) DNA content and cell cycle state of 162 cells growing on HGF-exposed ICAM1. (B) DAPI intensity of 58 replicating (EdU+) cells shows a bimodal distribution, indicating the presence of multiple subpopulations with different DNA content. (C) Arms race between the grower's energetic sensitivity (y-axis) and the goer's chemotactic ability (x-axis) reduces infiltration distance (color bar). A red circle outlines parameter combinations of interest explored in (D-F). (D-F) Spatial distribution of goer and grower for parameter values outlined in (C). (D) High chemotactic motility will cause the goer to leave the center of the dish too soon, leaving room for the grower to expand locally. (E) With an intermediate motility the goer succeeds maintaining its dominance both at the center and edge of the dish. (F) Low motility will prevent the goer from gaining a sufficient spatial lead from the grower while energy is still abundant, and it will lose dominance at the edge of the dish once energy becomes sparse. Red arrows indicate maximum infiltration distance achieved by either of the two populations.

MEMA spot has a low capacity, whereby confluence is reached at no more than a few hundreds of cells. Such a small number of cells will not exhibit wave-like behavior and therefore will not suffice for spatial structure to emerge. We therefore extended temporal and spatial domains, seeding cells at a lower confluence and letting them grow onto the entire energy domain until they consume all available energy (average of 127 days; Table 1).

We observed a non-monotonic relation between the goer's chemotactic ability and the speed with which the metapopulation invades the dish, with intermediate values being the least beneficial to its growth and spread (Fig. 4C). Temporal analysis of the simulations (Supplementary Data 1-3), revealed that if the goer's chemotactic motility is too high, it will leave the center of the dish too soon, leaving room for the grower to expand locally (Fig. 4D). By contrast, if the goer's motility is too low, it will miss the time-window of opportunity to ensure its dominance further away from the center

of the dish while energy is still abundant. As a consequence, it will be outgrown by the grower at the edge of the dish once energy becomes sparse (Fig. 4E). Only when the goer has an intermediate motility, does the grower persistently coexist with it, both at the center and edge of the dish (Fig. 4F). If high ploidy is indeed a characteristic specific to goer-like cells, then mTOR-Is are likely affecting this cell type (Fig. 1A,E,F), and could be used to inhibit its chemotactic response, thereby moving the meta-population up the x-axis of Fig. 4C.

Discussion

Models of infiltration are typically formulated under two critical assumptions. First, that energy production and consumption are non-uniform, leading to the formation of an energy gradient [51–53]; or second, that energy consumption is very slow compared to production, leading to an essentially infinite energetic resource [54].

Kimmel *et al.*

Here we formulate a generalized model of infiltration when energy is finite and investigate its behavior along a spectrum of scenarios, from permanent energy uniformity to scenarios where this uniformity is gradually lost. When energy is uniformly distributed at all times and the time scale for cell death is substantially longer than that of cell motility, our results suggests that the degree of infiltration can be approximated using the cells' density at equilibration of movement and growth (Fig. 2C).

With an energy gradient that becomes steeper over time, our analytical approximations no longer hold, as directed cell movement becomes non-negligible. For this scenario we leveraged MEMA profiling to inform regions of interest in the parameter search space. These regions of interest are relevant for cellular growth on a variety of HGF exposed ECM proteins. Simulations which ran at either high or low energy sensitivity (Fig. 3I) best resembled the observed growth patterns on the ECMs, giving rise to a bimodal distribution of meaningful model parameter values. The most intuitive explanation for this bimodal distribution are differences in ECM content. However, the distribution of energy sensitivity remained bimodal even across replicates of the same ECM, highlighting the possibility that it is not only the environment (i.e. the ECM) that varies across MEMA spots, but also the cell composition. An alternative explanation is that this variability stems from artifacts that arise during non-uniform printing of ECMs onto the array—the so called ring effect. However, a bimodal distribution was also observed in the DNA content of replicating cells, which is not affected by potential printing artifacts. The second peak of this bimodal distribution was wider, consistent with the fact that high-ploidy cells with more DNA need longer to replicate.

The cell line HCC1954 is described as a hyper-tetraploid cell line with an average DNA-content of 4.2 [37]. However, this average value may be misleading, as suggested by stark variability in nuclei sizes (Fig. 4A). Despite a wealth of genomic information generated for this cell line [37], to the best of our knowledge no prior reports indicate whether or not the cell line is polyploid. We and others have found that high ploidy is an aneuploidy-tolerating state that accompanies intra-tumor heterogeneity *in vivo* and *in vitro* [17, 55, 56]. Our results suggest that HCC1954 is likely polyploid.

If spatial and temporal domains were to be extended beyond the configuration of MEMA spots, our simulations predict that spatial segregation of two co-existing subpopulations according to their ploidy is a likely scenario and depends on the energy consumption rate. While our model can easily be extended to more than two subpopulations, it currently does not incorporate mutations, i.e. the process of generating new clonal lines. A next step will be to extend our model to include mutation events, specifically chromosome mis-segregations that contribute extensively to diversify ploidy of a population [31, 32]. The additional DNA content of high-ploidy cells, though energetically costly, brings a masking effect against the deleterious consequences of chromosome losses [22]. This duality may explain the higher sensitivity to glycolysis inhibitors of high-ploidy cells and their lower sensitivity to cytotoxic drugs previously reported in Glioblastoma [57].

In line with prior reports we find that increased resistance of breast cancer cell lines to cytotoxic drugs is associated with high ploidy. In contrast, high ploidy breast cancer cell lines were sensitive to inhibitors of signal transduction pathways, including EGFR and especially MTOR signalling. A commonality among those pathways is their contribution to a cell's chemotactic response [2, 58, 59], suggesting opportunities to tune chemotaxis. Delaying chemotactic response of highly chemotactic cells could slow down invasion by maximizing competition within a polyploid population. If on the other hand chemotactic response of high ploidy cells is already at an intermediate level, our simulation suggest that further reduction may accelerate invasion of low ploidy cells. For such scenarios therapeutic strategies that include an MTOR-I may not be successful. Experiments will be needed to verify these *in-silico* results *in-vitro*. Knowing how co-existing clones with differential drug sensitivities segregate spatially can offer opportunities to administer these drug combinations more effectively.

Acknowledgements

This work was supported by the National Cancer Institute R00CA215256 awarded to NA. PMA acknowledges support through the National Cancer Institute, part of the National Institutes of Health, under grant number P30-CA076292. The content is solely the responsibility of the authors and does not necessarily represent the official views of the National Institutes of Health or the H. Lee Moffitt Cancer Center and Research Institute.

References

- Spiteri I, Caravagna G, Cresswell GD, Vatsiou A, Nichol D, Acar A, et al. Evolutionary dynamics of residual disease in human glioblastoma. *Annals of Oncology: Official Journal of the European Society for Medical Oncology*. 2019;30(3):456–463.
- Gulhati P, Bowen KA, Liu J, Stevens PD, Rychahou PG, Chen M, et al. mTORC1 and mTORC2 regulate EMT, motility, and metastasis of colorectal cancer via RhoA and Rac1 signaling pathways. *Cancer Research*. 2011 May;71(9):3246–3256.
- Rotundo MS, Galeano T, Tassone P, Tagliaferri P. mTOR inhibitors, a new era for metastatic luminal HER2-negative breast cancer? A systematic review and a meta-analysis of randomized trials. *Oncotarget*. 2016 May;7(19):27055–27066.
- Liu L, Li F, Cardelli JA, Martin KA, Blenis J, Huang S. Rapamycin inhibits cell motility by suppression of mTOR-mediated S6K1 and 4E-BP1 pathways. *Oncogene*. 2006 Nov;25(53):7029–7040.
- Parr C, Watkins G, Mansel RE, Jiang WG. The hepatocyte growth factor regulatory factors in human breast cancer. *Clinical Cancer Research: An Official Journal of the American Association for Cancer Research*. 2004 Jan;10(1 Pt 1):202–211.
- Hynes RO. Extracellular matrix: not just pretty fibrils. *Science (New York, NY)*. 2009 Nov;326(5957):1216–1219. Available from: <https://www.ncbi.nlm.nih.gov/pmc/articles/PMC3536535/>.
- Liotta LA. Tumor invasion and metastases—role of the extracellular matrix: Rhoads Memorial Award lecture. *Cancer Research*. 1986 Jan;46(1):1–7.
- Aznavoorian S, Stracke ML, Kruttsch H, Schiffmann E, Liotta LA. Signal transduction for chemotaxis and haptotaxis by matrix molecules in tumor cells. *The Journal of Cell Biology*. 1990 Apr;110(4):1427–1438.
- Stupack DG, Cheresh DA. Get a ligand, get a life: integrins, signaling and cell survival. *Journal of Cell Science*. 2002 Oct;115(Pt 19):3729–3738.
- Parise LV, Lee J, Juliano RL. New aspects of integrin signaling in cancer. *Seminars in Cancer Biology*. 2000 Dec;10(6):407–414.
- Keenan AB, Jenkins SL, Jagodnik KM, Koplev S, He E, Torre D, et al. The Library of Integrated Network-Based Cellular Signatures NIH Program: System-Level Cataloging of Human Cells Response to Perturbations. *Cell Systems*. 2018;6(1):13–24.
- Lin CH, Lee JK, LaBarge MA. Fabrication and use of microenvironment microarrays (MEArrays). *Journal of Visualized Experiments: JoVE*. 2012 Oct;(68).
- Kuang W, Deng Q, Deng C, Li W, Shu S, Zhou M. Hepatocyte growth factor induces breast cancer cell invasion via the PI3K/Akt and p38 MAPK signaling pathways to up-regulate the expression of COX2. *American Journal of Translational Research*. 2017 Aug;9(8):3816–3826. Available from: <https://www.ncbi.nlm.nih.gov/pmc/articles/PMC5575195/>.
- Brastianos PK, Carter SL, Santagata S, Cahill DP, Taylor-Weiner A, Jones RT, et al. Genomic Characterization of Brain Metastases Reveals Branched Evolution and Potential Therapeutic Targets. *Cancer Discovery*. 2015 Nov;5(11):1164–1177. 00040.
- Angelova M, Mlecnik B, Vasaturo A, Bindea G, Fredriksen T, Lafontaine L, et al. Evolution of Metastases in Space and Time under Immune Selection. *Cell*. 2018 Oct;175(3):751–765.e16. Available from: <http://www.sciencedirect.com/science/article/pii/S0092867418312303>.
- Hannibal RL, Chuong EB, Rivera-Mulia JC, Gilbert DM, Valouev A, Baker JC. Copy number variation is a fundamental aspect of the placental genome. *PLoS genetics*. 2014 May;10(5):e1004290.
- Dewhurst SM, McGranahan N, Burrell RA, Rowan AJ, Grönroos E, Endesfelder D, et al. Tolerance of whole-genome doubling propagates chromosomal instability and accelerates cancer genome evolution. *Cancer Discovery*. 2014 Feb;4(2):175–185. 00068.
- Bielski CM, Zehir A, Penson AV, Donoghue MTA, Chatila W, Armenia J, et al. Genome doubling shapes the evolution and prognosis of advanced cancers. *Nature genetics*. 2018 Aug;50(8):1189–1195. Available from: <https://www.ncbi.nlm.nih.gov/pmc/articles/PMC6072608/>.
- Amend SR, Torga G, Lin KC, Kostecka LG, Marzo Ad, Austin RH, et al. Polyploid giant cancer cells: Unrecognized actuators of tumorigenesis, metastasis, and resistance. *The Prostate*. 2019;79(13):1489–1497. _eprint: <https://onlinelibrary.wiley.com/doi/pdf/10.1002/pros.23877>. Available from: <https://onlinelibrary.wiley.com/doi/abs/10.1002/pros.23877>.
- Pienta KJ, Hammarlund EU, Axelrod R, Brown JS, Amend SR. Poly-aneuploid cancer cells promote evolvability, generating lethal cancer. *Evolutionary Applications*;n/a(n/a). _eprint: <https://onlinelibrary.wiley.com/doi/pdf/10.1111/eva.12929>. Available from: <https://onlinelibrary.wiley.com/doi/abs/10.1111/eva.12929>.
- Zhang S, Mercado-Urbe I, Xing Z, Sun B, Kuang J, Liu J. Generation of cancer stem-like cells through the formation of polyploid giant cancer cells. *Oncogene*. 2014 Jan;33(1):116–128.
- López S, Lim EL, Horswell S, Haase K, Huebner A, Dietzen M, et al. Interplay between whole-genome doubling and the

Kimmel *et al.*

- accumulation of deleterious alterations in cancer evolution. *Nature Genetics*. 2020 Mar;52(3):283–293.
23. Pirkmajer S, Chibalin AV. Serum starvation: caveat emptor. *American Journal of Physiology-Cell Physiology*. 2011 May;301(2):C272–C279. Available from: <https://www.physiology.org/doi/full/10.1152/ajpcell.00091.2011>.
24. Growth of human diploid cells (strain MRC-5) in defined medium; replacement of serum by a fraction of serum ultrafiltrate. - PubMed - NCBI. Available from: <https://www.ncbi.nlm.nih.gov/pubmed/422676>.
25. Bartholomew JC, Yokota H, Ross P. Effect of serum on the growth of balb 3T3 A31 mouse fibroblasts and an SV40-transformed derivative. *Journal of Cellular Physiology*. 1976 Jul;88(3):277–286. Available from: <https://onlinelibrary.wiley.com/doi/10.1002/jcp.1040880303>.
26. Cai W, Rook SL, Jiang ZY, Takahara N, Aiello LP. Mechanisms of hepatocyte growth factor-induced retinal endothelial cell migration and growth. *Investigative Ophthalmology & Visual Science*. 2000 Jun;41(7):1885–1893.
27. Hatzikirou H, Basanta D, Simon M, Schaller K, Deutsch A. 'Go or grow': the key to the emergence of invasion in tumour progression? *Mathematical medicine and biology: a journal of the IMA*. 2012 Mar;29(1):49–65.
28. Kathagen-Buhmann A, Schulte A, Weller J, Holz M, Herold-Mende C, Glass R, et al. Glycolysis and the pentose phosphate pathway are differentially associated with the dichotomous regulation of glioblastoma cell migration versus proliferation. *Neuro-Oncology*. 2016 Sep;18(9):1219–1229. Available from: <https://www.ncbi.nlm.nih.gov/pmc/articles/PMC4998991/>.
29. Dhruv HD, McDonough Winslow WS, Armstrong B, Tuncali S, Eschbacher J, Kislin K, et al. Reciprocal Activation of Transcription Factors Underlies the Dichotomy between Proliferation and Invasion of Glioma Cells. *PLoS ONE*. 2013 Aug;8(8):e72134. 00009. Available from: <http://dx.doi.org/10.1371/journal.pone.0072134>.
30. Vittadello ST, McCue SW, Gunasingh G, Haass NK, Simpson MJ. Examining Go-or-Grow Using Fluorescent Cell-Cycle Indicators and Cell-Cycle-Inhibiting Drugs. *Biophysical Journal*. 2020 Mar;118(6):1243–1247. Available from: <http://www.sciencedirect.com/science/article/pii/S0006349520301119>.
31. Laughney AM, Elizalde S, Genovese G, Bakhoum SF. Dynamics of Tumor Heterogeneity Derived from Clonal Karyotypic Evolution. *Cell Reports*. 2015 Aug;12(5):809–820.
32. Elizalde S, Laughney AM, Bakhoum SF. A Markov chain for numerical chromosomal instability in clonally expanding populations. *PLoS computational biology*. 2018;14(9):e1006447.
33. Wang CH, Martin S, George AB, Korolev KS. Pinned, locked, pushed, and pulled traveling waves in structured environments. *Theoretical Population Biology*. 2019;127:102–119.
34. Bayliss A, Volpert VA. Complex predator invasion waves in a Holling–Tanner model with nonlocal prey interaction. *Physica D: Nonlinear Phenomena*. 2017 May;346:37–58. Available from: <http://www.sciencedirect.com/science/article/pii/S016727891630481X>.
35. Wasserstein L. Markov processes over denumerable products of spaces describing large systems of automata. 1969 Jan; Available from: <https://scinapse.io/papers/51701124>.
36. Sanderson C, Curtin R. Armadillo: a template-based C++ library for linear algebra. *Journal of Open Source Software*. 2016 Jun;1(2):26. Available from: <https://joss.theoj.org/papers/10.21105/joss.00026>.
37. van der Meer D, Barthorpe S, Yang W, Lightfoot H, Hall C, Gilbert J, et al. Cell Model Passports—a hub for clinical, genetic and functional datasets of preclinical cancer models. *Nucleic Acids Research*. 2019 Jan;47(D1):D923–D929. Publisher: Oxford Academic. Available from: <https://academic.oup.com/nar/article/47/D1/D923/5107576>.
38. Barretina J, Caponigro G, Stransky N, Venkatesan K, Margolin AA, Kim S, et al. The Cancer Cell Line Encyclopedia enables predictive modelling of anticancer drug sensitivity. *Nature*. 2012 Mar;483(7391):603–607. 00591. Available from: <http://www.nature.com/nature/journal/v483/n7391/full/nature11003.html>.
39. Heiser LM, Sadanandam A, Kuo WL, Benz SC, Goldstein TC, Ng S, et al. Subtype and pathway specific responses to anticancer compounds in breast cancer. *Proceedings of the National Academy of Sciences of the United States of America*. 2012 Feb;109(8):2724–2729.
40. Daemen A, Griffith OL, Heiser LM, Wang NJ, Enache OM, Sanborn Z, et al. Modeling precision treatment of breast cancer. *Genome Biology*. 2013;14(10):R110.
41. Bräutigam K, Mitzlaff K, Uebel L, Köster F, Polack S, Pervan M, et al. Subtypes of Triple-negative Breast Cancer Cell Lines React Differently to Eribulin Mesylate. *Anticancer Research*. 2016 Jun;36(6):2759–2766.
42. Dai X, Cheng H, Bai Z, Li J. Breast Cancer Cell Line Classification and Its Relevance with Breast Tumor Subtyping. *Journal of Cancer*. 2017 Sep;8(16):3131–3141. Available from: <https://www.ncbi.nlm.nih.gov/pmc/articles/PMC5665029/>.
43. Hänzelmann S, Castelo R, Guinney J. GSVA: gene set variation analysis for microarray and RNA-Seq data. *BMC Bioinformatics*. 2013 Jan;14(1):7. Available from: <https://doi.org/10.1186/1471-2105-14-7>.

44. Croft D, Mundo AF, Haw R, Milacic M, Weiser J, Wu G, et al. The Reactome pathway knowledgebase. *Nucleic Acids Research*. 2014 Jan;42(Database issue):D472–D477. Available from: <https://www.ncbi.nlm.nih.gov/pmc/articles/PMC3965010/>.
45. Hafner M, Niepel M, Chung M, Sorger PK. Growth rate inhibition metrics correct for confounders in measuring sensitivity to cancer drugs. *Nature Methods*. 2016;13(6):521–527.
46. Hafner M, Heiser LM, Williams EH, Niepel M, Wang NJ, Korkola JE, et al. Quantification of sensitivity and resistance of breast cancer cell lines to anti-cancer drugs using GR metrics. *Scientific Data*. 2017 Nov;4. Available from: <https://www.ncbi.nlm.nih.gov/pmc/articles/PMC5674849/>.
47. Yang W, Soares J, Greninger P, Edelman EJ, Lightfoot H, Forbes S, et al. Genomics of Drug Sensitivity in Cancer (GDSC): a resource for therapeutic biomarker discovery in cancer cells. *Nucleic Acids Research*. 2013 Jan;41(Database issue):D955–D961. Available from: <https://www.ncbi.nlm.nih.gov/pmc/articles/PMC3531057/>.
48. Chen WYJ, Abatangelo G. Functions of hyaluronan in wound repair. *Wound Repair and Regeneration*. 1999;7(2):79–89. Available from: <https://onlinelibrary.wiley.com/doi/abs/10.1046/j.1524-475X.1999.00079.x>.
49. Ellis IR, Schor SL. Differential effects of TGF-beta1 on hyaluronan synthesis by fetal and adult skin fibroblasts: implications for cell migration and wound healing. *Experimental Cell Research*. 1996 Nov;228(2):326–333.
50. Fisher RA. THE WAVE OF ADVANCE OF ADVANTAGEOUS GENES. *Annals of Eugenics*. 1937 Jun;7(4):355–369. Available from: <http://doi.wiley.com/10.1111/j.1469-1809.1937.tb02153.x>.
51. Lim S, Nam H, Jeon JS. Chemotaxis Model for Breast Cancer Cells Based on Signal/Noise Ratio. *Biophysical Journal*. 2018;115(10):2034–2043.
52. Keller EF, Segel LA. Model for chemotaxis. *Journal of Theoretical Biology*. 1971 Feb;30(2):225–234. Available from: <http://www.sciencedirect.com/science/article/pii/0022519371900506>.
53. Anderson ARA, Rejniak KA, Gerlee P, Quaranta V. Microenvironment driven invasion: a multiscale multimodel investigation. *Journal of mathematical biology*. 2009 Apr;58(4-5):579–624. Available from: <https://www.ncbi.nlm.nih.gov/pmc/articles/PMC5563464/>.
54. Kimmel GJ, Gerlee P, Altrock PM. Time scales and wave formation in non-linear spatial public goods games. *PLOS Computational Biology*. 2019 Sep;15(9):e1007361. Publisher: Public Library of Science. Available from: <https://journals.plos.org/ploscompbiol/article?id=10.1371/journal.pcbi.1007361>.
55. Andor N, Simonds EF, Czerwinski DK, Chen J, Grimes SM, Wood-Bouwens C, et al. Single-cell RNA-Seq of lymphoma cancers reveals malignant B cell types and co-expression of T cell immune checkpoints. *Blood*. 2018 Jan;p. blood–2018–08–862292. Available from: <http://www.bloodjournal.org/content/early/2018/12/26/blood-2018-08-862292>.
56. Birkbak NJ, Eklund AC, Li Q, McClelland SE, Endesfelder D, Tan P, et al. Paradoxical relationship between chromosomal instability and survival outcome in cancer. *Cancer research*. 2011 May;71(10):3447–3452. 00068 PMID: 21270108.
57. Donovan P, Cato K, Legaie R, Jayalath R, Olsson G, Hall B, et al. Hyperdiploid tumor cells increase phenotypic heterogeneity within Glioblastoma tumors. *Molecular bioSystems*. 2014 Jan;.
58. Bailly M, Wyckoff J, Bouzahzah B, Hammerman R, Sylvestre V, Cammer M, et al. Epidermal Growth Factor Receptor Distribution during Chemotactic Responses. *Molecular Biology of the Cell*. 2000 Nov;11(11):3873–3883. Available from: <https://www.ncbi.nlm.nih.gov/pmc/articles/PMC15043/>.
59. James RG, Davidson KC, Bosch KA, Biechele TL, Robin NC, Taylor RJ, et al. WIKI4, a novel inhibitor of tankyrase and Wnt/ β -catenin signaling. *PloS One*. 2012;7(12):e50457.